Wide frequency range measurements of absolute phase and amplitude of vibrations in micro- and nanostructures by optical interferometry

Hanne Martinussen, Astrid Aksnes and Helge E. Engan

Norwegian University of Science and Technology (NTNU),
Department of Electronics and Telecommunications,
Trondheim, Norway

hanne.martinussen@iet.ntnu.no

Abstract: A heterodyne interferometer has been built in order to characterize vibrations on micro- and nanostructures. The interferometer offers the possibility of both absolute phase and high resolution absolute amplitude vibrational measurements. By using two acousto-optic modulators (AOMs) in one of the interferometer arms and varying the frequency inputs of both, the setup is designed to measure vibrations in the entire frequency range 0 - 1.2GHz. The system is here demonstrated on Capacitor Micromachined Ultrasonic Transducers (CMUTs) and a PZT transducer to show measurements from 5kHz up to 35MHz. We have measured absolute amplitudes with picometer resolution.

© 2007 Optical Society of America

OCIS codes: (120.3940) Metrology; (120.3180) Interferometry; (120.4290) Nondestructive testing

---

References and links

1. K. Midtbø, A. Rønnekleiv, D. T. Wang, "Fabrication and characterization of CMUTs realized by wafer bonding," in Proceedings of IEEE Ultrasonics Symp. (IEEE, 2006), pp. 934-937.
2. K. Kokkonen, J. V. Knuuttila, V. P. Plessky and Martti M. Salomaa, "Phase-sensitive absolute-amplitude measurements of surface waves using heterodyne interferometry," in Proceedings of IEEE Ultrasonics Symp. (IEEE, 2003), pp. 1145-1148.
3. J. Lawall, E. Kessler, "Michelson interferometry with 10 pm accuracy," Review of Scientific Instruments **71**, 2669–2676 (2000).
4. T. Chiba, "Amplitude and phase measurement of surface acoustic waves within a SAW filter having fan-shaped transducers and numerical simulations," in Proceedings of IEEE Ultrasonics Symp. (IEEE, 2005), pp. 1584-1587.
5. C. Gorecki, "Sub-micrometric displacement measurements by an all-fiber laser heterodyne interferometer using digital phase demodulation," J. Optics (Paris) **vol. 26**, 29–34 (1995).
6. J. E. Graebner, B. P. Barber, P. L. Gammel, and D. S. Greywall, "Dynamic visualization of subångstrom high-frequency surface vibration," Appl. Phys. Lett. **78**, 159–161 (2001).
7. H. Martinussen, A. Aksnes, H. E. Engan, "Heterodyne Interferometry for high sensitivity absolute amplitude vibrational measurements," Proc. SPIE **6292**, 0Z1-0Z11 (2006).
8. A. Aksnes, H. Martinussen, H. E. Engan, "Characterization of acoustic vibrations on micro- and nanostructures with picometer sensitivity," Proc. SPIE **6293**, 0A1-0A12 (2006).
9. P. Hariharan, *Basics of interferometry* (Academic Press, Inc., USA, 1992).

---

1. Introduction

Micro-Electro-Mechanical Systems (MEMS) and nanostructures have become important devices as demands on functionality and smaller products are increasing. MEMS-devices are being used as filters, ultrasound transducers, Digital Micrometer Devices (DMDs) etc. The design and fabrication processes associated with these small devices are complicated, and many uncontrolled errors may occur. It is crucial to be able to perform non-destructive evaluation and characterization of these devices. Important parameters to measure are the phase and amplitudes of nano- to picometer range vibrations. Once these parameters are determined, possible errors can be revealed and compensated for.

At our department Capacitor Micromachined Ultrasonic Transducers (CMUTs) are being developed and fabricated [1] to be integrated into a 1mm diameter intravascular ultrasound (IVUS) catheter. The dimensions of the CMUTs are from 5.7μm to 11.4μm in radius, and the deflection amplitude of the vibrating membrane is in the sub-nanometer to nanometer range. During process development of these CMUTs it is important to perform quality control of the vibration patterns. Research using heterodyne [2] , [3] , [4] , [5] and homodyne [6] interferometer techniques to perform highly sensitive characterization measurements has been described in recent literature. Heterodyne interferometry is obtained by introducing a frequency shift in one of the interferometric arms. This technique permits direct measurements of absolute amplitude and phase with high resolution and low noise. This paper presents a heterodyne interferometer to perform simultaneous absolute amplitude and phase measurements of the vibration, using two acousto-optic modulators (AOMs) [7] , [8]. Our setup requires a high frequency detector, whereas the rest of the signal processing is handled in the low frequency range. Anticipating requests for measurements at considerably higher and lower frequencies in future projects, we have developed a flexible setup designed to measure in the entire frequency range from 0 to 1.2GHz. So far we have obtained a noise floor of 6pm amplitude at 31MHz with detection bandwidth 3.3Hz. No commercial equipment is, to our knowledge, covering this amplitude and frequency range with similar specifications.

2. Theory and experimental setup

2.1. The optical setup

The experimental setup is shown in Fig. 1. A linearly polarized 532nm Diode Pumped Solid State (Coherent Verdi V-2) laser is used. The following polarizing beam splitter (PBS) reflects vertically polarized and transmits horizontally polarized light. The frequency shift in the reference arm is obtained by using two AOMs. The AOMs have a frequency range of 200±100MHz. When the two AOMs are oriented with the input RF signal in opposite directions, the total frequency shift is the difference between the two AOM frequencies and therefore can be tuned between 0 and 200MHz. When both AOMs are oriented to introduce an upshift in frequency, the total frequency shift can be tuned from 200 to 600MHz. Since the concept determines the sample modulation frequencies to be twice the total frequency shift in the reference arm, our setup is designed to measure vibrations in the entire frequency range of 0-1.2GHz. This property is discussed in more detail in section 2.3. If there are requirements on characterizing devices driven at higher frequencies, this can in principle be obtained by substituting the AOMS with those having higher frequency.

In the object arm the light is focused on the sample with a microscope objective, and reflected the same way back. By passing twice through the quarter wave retarder, horizontally polarized light is transformed into vertically polarized light. Because vertically polarized light is reflected from the PBS no light is reflected back to the laser. The light beam in the reference arm and object arm are recombined with the beam splitter (BS) and interferes on the avalanche photo-
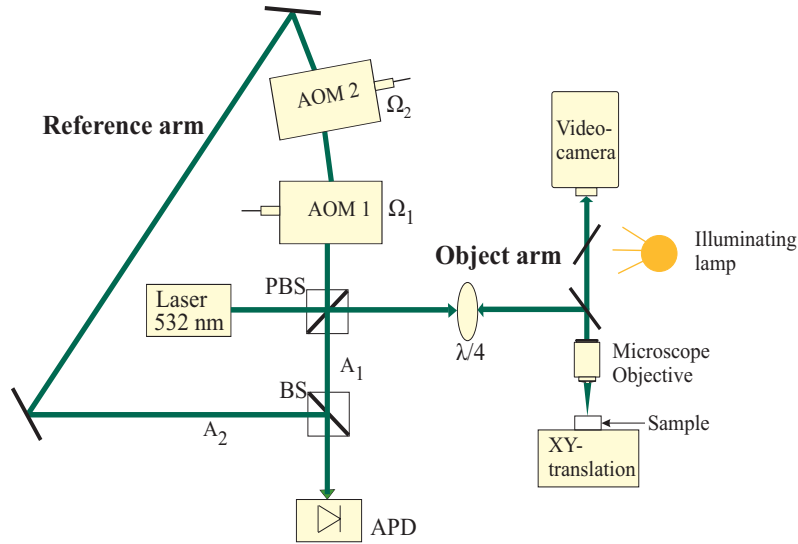
Fig. 1. The heterodyne interferometer.

diode (APD). The gain of the APD is controlled externally with a DC voltage supply to ensure constant gain at all measurements. The microscope objective with numerical aperture NA=0.55 yields a lateral resolution of 0.8μm. If needed, the microscope objective can be changed to meet other requirements of lateral resolution. The sample is placed on a Newport motorized XY-translation table with lateral resolution of 0.1μm.

2.2. The electrical setup

Figure 2 shows the electrical system used in our setup. Two signal generators are used to excite the acousto-optic modulators at frequencies Ω_1 and Ω_2. One signal generator is used to excite the sample under test at frequency Ω_a. A fourth signal generator, also operated at Ω_a, is mixed with the first two generators to obtain a coherent reference signal. When this product is mixed with a signal generator operated at $\Omega_{mix(I)}$, the reference signal is mixed down to $\Delta\Omega$=1kHz. As can be seen from the sketch the detector signal from the APD is split into two by a 3dB power splitter. The two last generators, operating at $\Omega_{mix(I)}$ (I for information signal) and $\Omega_{mix(N)}$(N for normalizing signal), are each mixed with the detector signal. Each mixer output is fed into a lock-in amplifier (LIA) and a PC controls that the recordings are done simultaneously from the two LIAs.

The two frequencies $\Omega_{mix(I)}$ and $\Omega_{mix(N)}$ are chosen appropriately to bring the information signal at $\Omega_a \pm (\Omega_2 - \Omega_1)$ and the normalizing signal at $\pm(\Omega_2 - \Omega_1)$ down to $\Delta\Omega$=1kHz. This is described more detailed in section 2.3.

The frequency difference between $\Omega_{mix(I)}$ and $\Omega_{mix(N)}$ is 4kHz. By keeping this difference small we are ensured approximately uniform response of the mixing process with the APD.

All signal generators are coupled to the same master generator to ensure that they are phase locked.

We foresee a simplification of the electrical part of the setup, an effort we have not yet pursued. All measurements in this article are performed with 3.3Hz bandwidth detection.
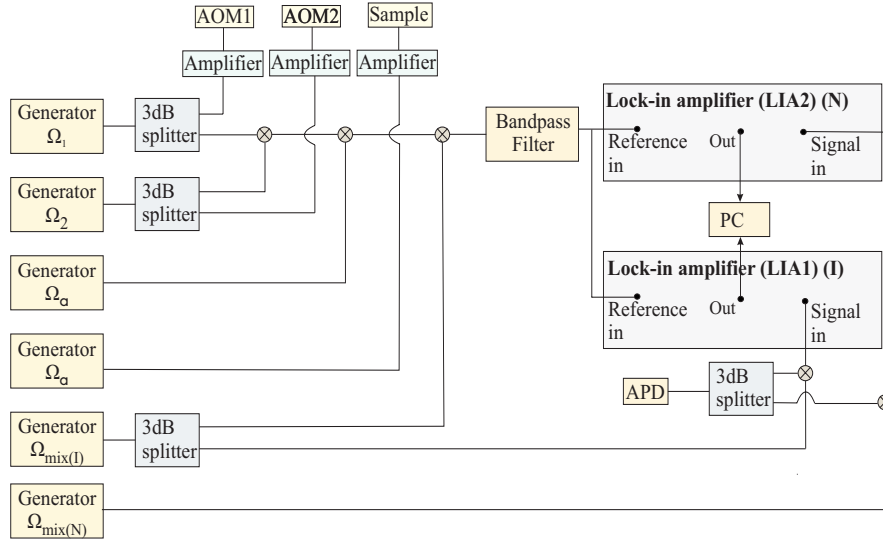
Fig. 2. The electrical system.

2.3. *Principles of absolute amplitude and phase measurements*

Absolute amplitude measurements

For the following derivation we assume that the setup is operated in the lower frequency mode where the combined frequency shift by the AOMs is $|\Omega_2 - \Omega_1|$. A similar derivation can be made for the upper frequency mode by using $\Omega_2 + \Omega_1$ as the frequency shift. For simplicity we define $\Omega_{mod} = |\Omega_2 - \Omega_1|$. To obtain a mathematical expression for the detector signal we add the electric fields in the two interferometer arms and take the absolute value squared. The electric fields in the object and reference arm are:

$$
\begin{aligned}
E_1(t) &= A_1 \cos[\omega_0 t + \phi_1], \\
E_2(t) &= A_2 \cos[(\omega_0 + \Omega_{mod})t + \phi_2].
\end{aligned}
\tag{1}
$$

A_i and ϕ_i denote the amplitudes and phases of the electromagnetic fields in the object (i=1) and reference arm (i=2), respectively (Fig. 1), ω_0 is the optical frequency. The detector signal without sample modulation is equal to:

$$
\begin{aligned}
I(t) \;\sim\; & \left(E_1(t) + E_2(t)\right)^2 \\
= \; & \frac{A_1^2}{2} + \frac{A_2^2}{2} \\
& + \frac{1}{2}\left\{A_1^2 \cos\left[2\omega_0 t + 2\phi_1\right] + A_2^2 \cos\left[2(\omega_0 + \Omega_{mod})t + 2\phi_2\right]\right\} \\
& + A_1 A_2 \cos\left[(2\omega_0 + \Omega_{mod})t + \phi_1 + \phi_2\right] \\
& + A_1 A_2 \cos\left[(\Omega_{mod})t - \phi_1 + \phi_2\right].
\end{aligned}
\tag{2}
$$

Because the detector in our setup is limited to frequencies below 1GHz, the optical frequencies cannot be detected. As a result, the only time-varying term in Eq. 2 which can be recorded is $A_1 A_2 \cos\left[(\Omega_{mod})t - \phi_1 + \phi_2\right]$, and thus, we can neglect the remaining terms in the further study.

We want to measure the vibration of the sample in Fig. 1. A vibration in the object arm with frequency Ω_a can be described as a time-varying phase modulation $\Delta\phi_1$ of the detector signal in Eq. 2 which is added to the ϕ_1 term and is equal to [9]:

$$\Delta\phi_1(t) = \frac{4\pi a}{\lambda}\cos(\Omega_a t + \phi),\qquad(3)$$

where a and ϕ are the amplitude and phase of the sample oscillation respectively, and λ is the laser wavelength. We assume the amplitude a to be smaller than $\frac{\lambda}{4}$. When the amplitudes are larger ambiguity may occur. The resulting expressions can be simplified using the Bessel functions. Whenever $\frac{4\pi a}{\lambda}$ is much smaller than unity, we can approximate the Bessel functions to the first order and obtain the following:

$$
\begin{aligned}
I(t) \;=\; & A_1 A_2 \cos\left[(\Omega_{mod})t - \phi_1 + \phi_2\right] \\
& + A_1 A_2 \frac{2\pi a}{\lambda}\sin\left[(\Omega_a - \Omega_{mod})t + \phi_1 - \phi_2 + \phi\right] \\
& + A_1 A_2 \frac{2\pi a}{\lambda}\sin\left[(\Omega_a + \Omega_{mod})t - \phi_1 + \phi_2 + \phi\right].
\end{aligned}\qquad(4)
$$

The Fourier Transform of $I(t)$, $I(f)$, is shown schematically in Fig. 3. As can be seen from the figure the vibration amplitude a is proportional to the amplitude of the signal with frequency $(\Omega_a - \Omega_{mod})$. Thus by doing two simultaneous measurements, one at the carrier frequency Ω_{mod} (denoted N, from normalizing signal), and one at the sideband frequency $(\Omega_a - \Omega_{mod})$ (denoted I from information signal), the combination of these two measurements yields the absolute value of the amplitude:

$$a = \frac{\lambda}{2\pi}\frac{R_I}{R_N}.\qquad(5)$$

R_I and R_N are the amplitude measurements of the information and normalizing signal, respectively.
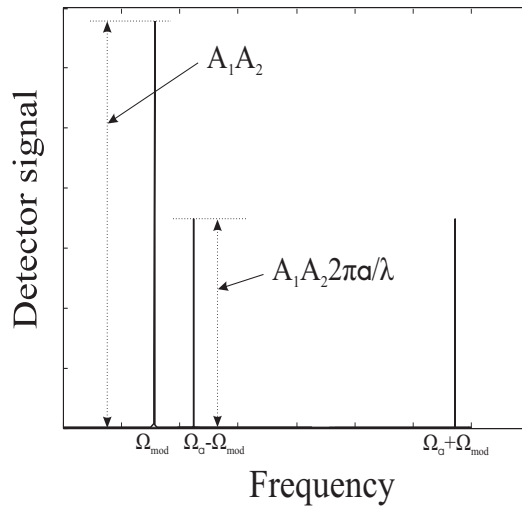

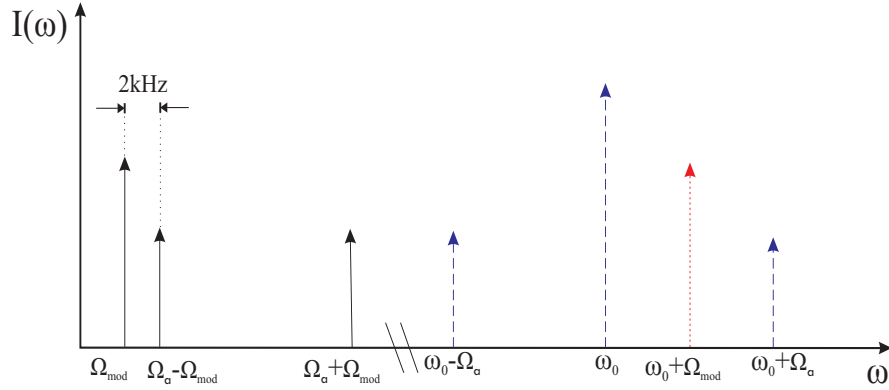Fig. 3. Fourier Transform of the detector signal.

Fig. 4. Frequency diagram of signal components in the interferometer.

Figure 4 shows a frequency diagram of the frequency components related to the interferometer. The blue arrows (broken lines) refer to the frequency components in the object arm of the interferometer whereas the red arrow (dotted line) refers to the frequency component in the reference arm. The black arrows (solid lines) refer to the frequency components resulting from the mixing of the components in the object and reference arm by the beam splitter (BS). In order to maintain approximately uniform frequency response of the mixing process in the APD we have decided the difference between Ω_{mod} and $\Omega_a - \Omega_{mod}$ to be 2kHz. This is done by defining the following:

$$\Omega_{mod} = \frac{\Omega_a}{2} - \Delta\Omega, \tag{6}$$

where $\Delta\Omega$ is equal to 1kHz. When both AOMs are oriented to achieve maximum frequency shift, $\Omega_{mod(max)}$ equals 600MHz. The maximum sample modulation frequency possible to measure with the setup is then:

$$\Omega_{a(max)} = 2 \cdot \Omega_{mod(max)} + 2 \cdot \Delta\Omega = 1200.002 MHz. \tag{7}$$

Phase measurements

The detector signal in Eq. 4 is, as previously discussed, split into one information signal (I) and one normalizing signal (N). The two signals are then each mixed with a signal generator having phases $\theta_{mix(I)}$ and $\theta_{mix(N)}$, respectively. After these mixing processes the signals are fed to two lock-in amplifiers where another mixing process is performed. After these last mixing processes in the LIAs the information and normalizing signals will have reference phases denoted $\theta_{ref(I)}$ and $\theta_{ref(N)}$, respectively. The SR830 dual lock-in amplifier used in the setup can retrieve the phase of the signal directly. The obtained phase signals of I and N are:

$$\phi_I = \phi_2 - \phi_1 - \phi + \theta_{mix(I)} + \theta_{ref(I)}, \tag{8}$$
$$\phi_N = \phi_2 - \phi_1 + \theta_{mix(N)} + \theta_{ref(N)}. \tag{9}$$

ϕ_1 and ϕ_2 denote the phases of the electromagnetic fields in the object and reference arm, respectively (Fig. 1). ϕ represents the phase of the vibration of the sample which we want to measure. ϕ_1 and ϕ_2 may lead to individual drift in the phase measurements (see section 3.1.2), but these parameters can be canceled out. Thus from the two last equations the estimated phase can be taken to be:

$$\phi_{est} = \phi_I - \phi_N = -\phi + \theta_{mix(I)} - \theta_{mix(N)} + \theta_{ref(I)} - \theta_{ref(N)}. \tag{10}$$

$\theta_{mix(I)}$, $\theta_{mix(N)}$, $\theta_{ref(I)}$ and $\theta_{ref(N)}$ are constant phases because all signal generators are locked to a master oscillator. The vibration phase can therefore be measured without being influenced by optical phase drift due to, for example, change in optical path lengths of the two interferometer arms or vertical movement of the sample surface. Thus apart from an arbitrary constant given by the electrical part of the setup absolute vibration phase can be measured with high stability.

3. Measurements

3.1. CMUTs

Two different CMUT structures were characterized. One structure has CMUT element radius of 5.7μm, the other 11.4μm. Figure 5(a) shows a microscope image of the entire CMUT matrix with connection pads to the columns. The CMUT elements in the microscope image are 11.4μm in radius and the whole matrix consists of 36x52 CMUTs. A scanning electron microscope image of a selection of 8 CMUTs is shown in Fig. 5(b). Two columns are interconnected and an applied RF signal excites all CMUTs connected. A sketch of one single CMUT membrane with 5.7μm radius is shown in Fig. 6. For the CMUT to transmit at the operating RF frequency a DC voltage has to be applied. This DC voltage causes a predeflection as indicated in Fig. 6 which increases the linear response.
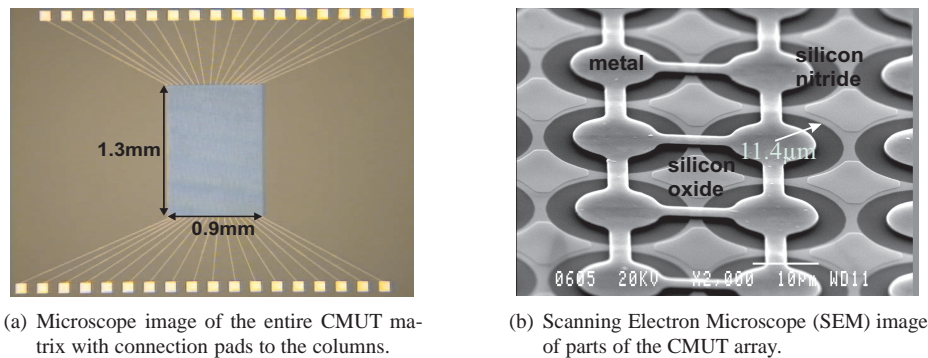

(a) Microscope image of the entire CMUT matrix with connection pads to the columns.

(b) Scanning Electron Microscope (SEM) image of parts of the CMUT array.

Fig. 5. Microscope images of the CMUT structure.

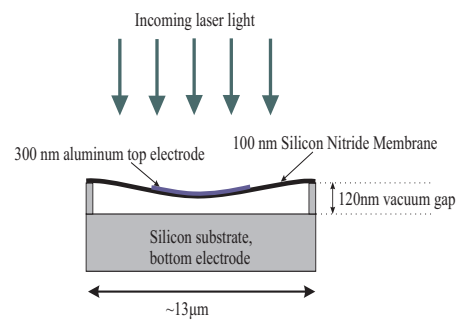
Fig. 6. Sketch of a 5.7μm radius CMUT.

3.1.1. Absolute amplitude measurements and investigation of linear response

We investigated the linearity of the response on the 5.7μm structure. The CMUT structure was biased with -20VDC and excited at 31.0MHz. Line scans were performed across the middle of CMUT(21,3) with RF excitation amplitudes between 4mV RMS and 12.6mV RMS. The position in the array is indicated by the two numbers in the parenthesis representing columns and rows, respectively. The results are shown in Fig. 7(a) and 7(b). Figure 7(b) is based on the mean value of the points -5μm, -6μm and -7μm from the line scans in Fig. 7(a). From the results we can see a very linear response. This simplifies requirements for the electronics of the ultrasound transducer.
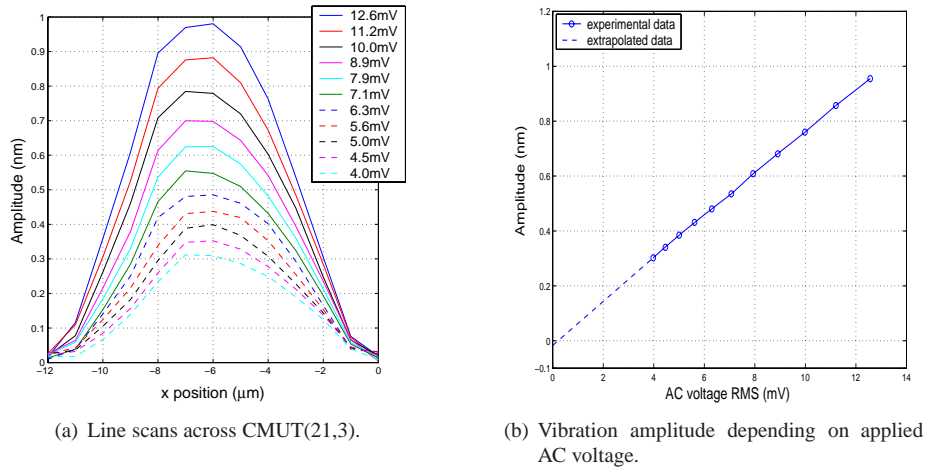

(a) Line scans across CMUT(21,3).

(b) Vibration amplitude depending on applied AC voltage.

Fig. 7. Investigation of linear response of the CMUT.

3.1.2. Phase measurements

We shall now verify the phase compensation scheme discussed in the theoretical part above. The phase information of the vibration is contained in the information signal. However, various factors may lead to drift of the phase of both the information (I) and the normalizing (N) signal. These factors can be divided into two. One is phase drift due to external causes and unrelated to the measurement process such as drift in ambient temperature, air turbulence and instabilities of the output power of the laser. The other factor is phase changes as a function of position caused by a tilt of the sample relative to the scanning direction. Both factors can be compensated for as shown below.

Figure 8(a) and 8(b) show uncorrected phase measurements of the information and normalizing recordings. They both correspond to the 12.6mV line scan in Fig. 7(a). The normalizing phase measurements contain no information about the vibration of the sample. They depend only on the term $\phi_2 - \phi_1$ of the optical path difference between the two interferometer arms due to external factors and to the tilt of the sample. The slope of the curves in both figures reflects changes in the optical path length of the object arm as we move the sample across the laser spot. This is due to the non-parallelism between the surface of the sample and the scanning direction. This is sketched in Fig. 9 where the difference in optical path length between the two edges of the sample is Δ. The same will occur if the surface of the sample has roughnesses and bumps. However, since the tilt also affects the phase measurements of the information signal (Fig. 8(a)) we are able to correct for the deviations this leads to simply by subtracting the two measurements.
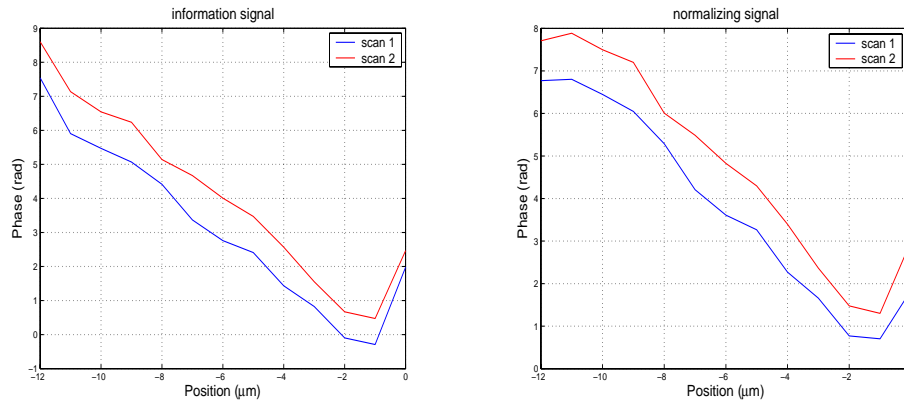
(a) Information signal phase measurements before any corrections.

(b) Normalizing phase measurements.

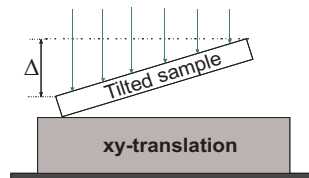Fig. 8. Phase measurements before any corrections.

Fig. 9. Tilted sample. When the sample is tilted the optical path length changes as the sample is moved by the translation table. In this sketch the maximum optical path difference is Δ between the two edges of the sample.

The phases of the two consecutive line scans shown in Fig. 8(b) have different values at a given position. This is due to the phase drift having contributions from external factors such as temperature fluctuations in the two interferometric arms. To identify phase drift due to external factors we measured at one point for 700 seconds as shown in Fig. 10(a) and 10(b). As can be seen from Fig. 10(a) the phase of the information signal (I) drifts over time. This can be compensated for by using the phase measurements of the normalized signal (N) which is drifting simultaneously with I. Figure 10(b) shows the phase corrected for drift as a function of time obtained by subtracting the phase of I from that of N. The RMS noise of the phase measurement is now 3.7°.

To summarize, we can correct for changes in optical path length whether they are due to stochastic effects such as temperature fluctuations or are caused by surface roughness and non-parallelism between the sample and the scanning direction. This is obtained by subtracting the phase of the normalizing signal from that of the information signal as prescribed in Eq. 10.

Corrected phase measurements corresponding to the line scans in Fig. 7(a) are demonstrated in Fig. 11. The measurements show that the phases have a flat curve in all of the line scans, confirming the conclusion we can draw from Fig. 7(a) that the CMUT is vibrating in the first harmonic mode. At one of the edges of the CMUT, corresponding to x=-12μm, the phases of all the scans increase with a mean phase of 1.3rad. This is thought due to the neighboring CMUT which is vibrating slightly out of phase compared to the one we are investigating. The reason for this is that the neighboring CMUT has a different resonance frequency than the one under inspection and this leads to phase differences in the vibration patterns. When animating
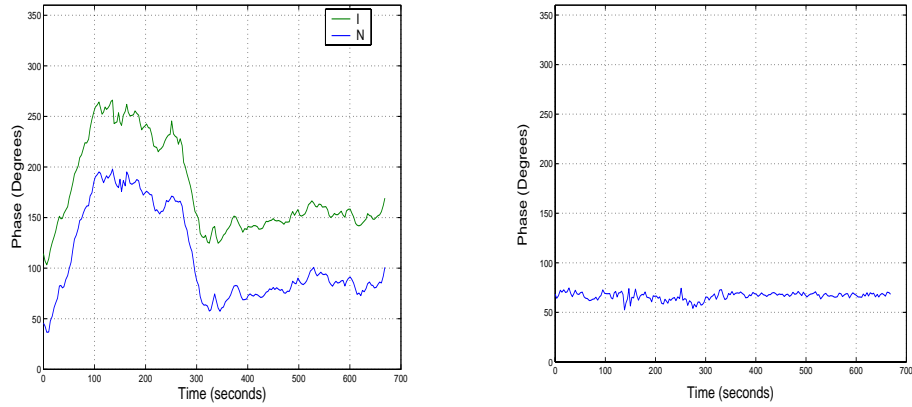
(a) Time drift of phase of I and N caused by external factors such as temperature fluctuations.

(b) Phase corrected for time drift caused by external factors.

Fig. 10. Phase measurements as a function of time.

the results in a movie, this can be clearly visualized as is shown in section 3.1.3. At x=0μm the phase measurements are seemingly random. The reason for this is that the vibration amplitude at this point is low and therefore the signal to noise ratio is low.
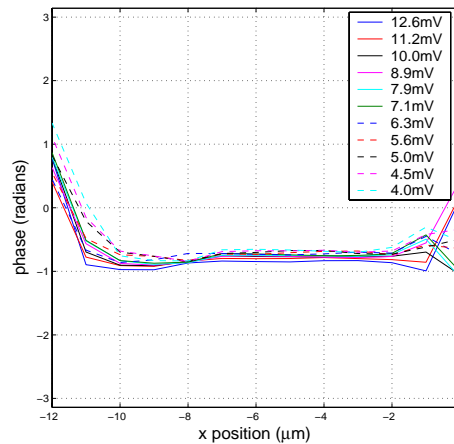

Fig. 11. Phase measurements as a function of AC RMS excitation performed at 31MHz and -20VDC.

3.1.3. 2D scan animation

With our setup we can perform 2D scans across a given field. By combining the absolute amplitude and phase measurements we can reconstruct the vibration pattern in a movie. The movies are shown in Fig. 12. This is a very powerful tool as the phase and amplitude relations between different elements are easily perceivable. In the multimedia-file attached the 11.4μm radius CMUT structure is excited at 13.9MHz and 14.0MHz to compare the vibration patterns at the two frequencies. The CMUTs excited are CMUT(3,5)-(3,7) and CMUT(4,5)-(4,7) with amplitude 177mV RMS. As can be seen from the movies, the CMUTs have different resonance frequencies. The movies also show how different elements vibrate with different phases

at frequency 13.9MHz, whereas they vibrate in phase at 14.0MHz. The movies demonstrate the ability of our setup to investigate and display various properties of different vibrating elements so they can be easily compared. The time employed for acquiring data for a 2D scan of this size is approximately 4 hours. The recording time can be decreased by optimizing the recording scheme further.

(a) Movie of the vibration pattern of 6CMUTs excited at 13.9MHz with 177mV RMS excitation amplitude.

(b) Movie of the vibration pattern of 6CMUTs excited at 14.0MHz with 177mV RMS excitation amplitude.
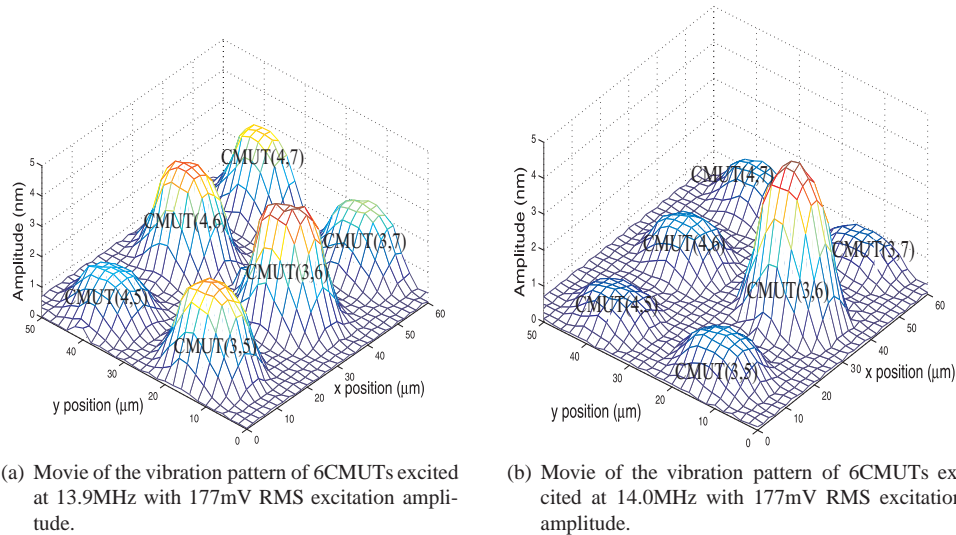
Fig. 12. Movies reconstructed from the amplitude and phase measurements. They demonstrate the vibration patterns of 6CMUTs excited at frequency 13.9MHz and 14.0MHz with 177mV RMS amplitude.

3.2. PZT transducer

To demonstrate the wide range of frequencies that can be measured by the setup, we include measurements on a device consisting of a Lead Zirconate Titanate (PZT) transducer onto which a mirror is glued to increase reflectivity (Fig. 13). Silver electrodes cover both sides of the transducer. Figure 14(a) shows a frequency scan of the transducer. The measurements are recorded from 5kHz to 300kHz in 5kHz steps and compared with simulations performed on a device with similar material properties as shown in Fig. 14. Note that the amplitude measurements are relative, as we are primarily interested in the general shape of the frequency curves. As can be seen from Fig. 14(a) the transducer has 5 distinct resonance peaks. The same 5 peaks can be identified at approximately the same frequencies in the simulation in Fig. 14(b). This shows that the measurements from our setup are in fair agreement with the simulations, in particular for the lower frequency band. The measured amplitudes of the resonances do not correspond to the simulated amplitudes, mainly due to uncertainties in material loss assumptions. In addition, it should be noted that the mirror has not been taken into account in the simulation.
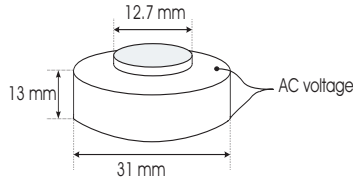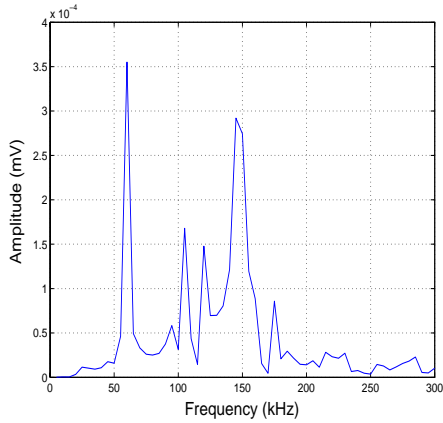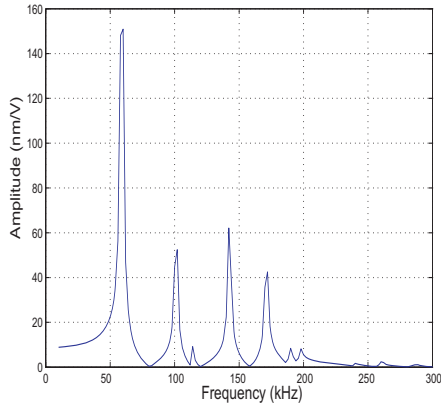
Fig. 13. Sketch of the PZT device.

(a) Frequency scan of PZT.

(b) Simulation of frequency scan of PZT device. The simulation is based on a pure crystal symmetry.

Fig. 14. Measurements and simulations on PZT device.

4. Sensitivity and noise floor

This section will demonstrate the smallest amplitude possible to measure with the setup described. The example is a line scan across the middle of CMUT(21,3) biased with -20VDC, excited with 0.4mV RMS at 31.0MHz frequency. Figure 15 shows the result from the scan. As can be seen from the figure, the maximum vibration amplitude of the CMUT at this low amplitude excitation is 24pm. We can identify dips on the curve due to the fact that we are approaching the noise floor of the setup. The line scan demonstrates the small details we can identify with our sensitive setup. From previous scans we have identified the noise floor to be approximately 6pm at 3.3Hz detection bandwidth. The noise floor is larger than the digitalization steps from the signal generators that are 2pm.

5. Limitations of the setup

5.1. Feedback in frequency mixers

We identified noise which arose from the electrical part of the setup. This mainly came from leakage in the electronic frequency mixers. The mixer leading to feedback is a Minicircuit ZAD3. The feedback problem is illustrated in Fig. 16. The signal from the signal generator
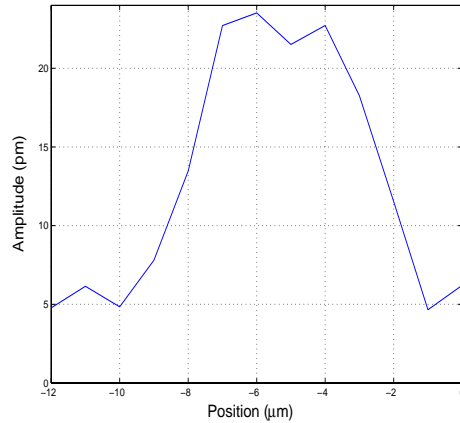
Fig. 15. Line scan across CMUT(21,3).

called $\Omega_{mix(N)}$ couples via the frequency mixer into the output of the 3dB power splitter, a Minicircuit ZMSC-2-2. The signal then couples into the other input, via a frequency mixer, and into the input of LIA1.

The frequency mixer is specified to have an input signal of 7dBm at the LO-input (Local Oscillator), and up to 1dBm on the RF-input (Radio Frequency). The signal generator called $\Omega_{mix(N)}$ has its output connected to the LO, and the signal from the APD has its input on the RF. The isolation between the LO- and the RF-input is $40dB$ according to the specifications of the mixer. From the specifications of the power splitter there is 30dB isolation between the two output ports. The initial signal from the signal generator $\Omega_{mix(N)}$ is 7dBm. Since there is 40dB isolation between LO- and RF input, -33dBm will couple out of the RF port of the mixer. Because of 30dB isolation between the output ports on the power splitter -63dBm will couple out of the opposite output port. This signal travels via the frequency mixer and into the input on the LIA1. In a 50Ω system this amplitude equals 0.15mV. If we compare to the data from the line scan in Fig. 15 the maximum amplitude equal to 24pm corresponds to an electric amplitude of 0.012mV. Thus, amplitudes in the tens of picometer range were not possible to measure with the setup arranged as in Fig. 16. The feedback amplitude corresponds to approximately 73pm, which would lead to a relatively high noise floor. Feedback from the signal generator called $\Omega_{mix(I)}$ into LIA2 is not a problem, since the signals fed into LIA2 are large compared to the feedback signal.
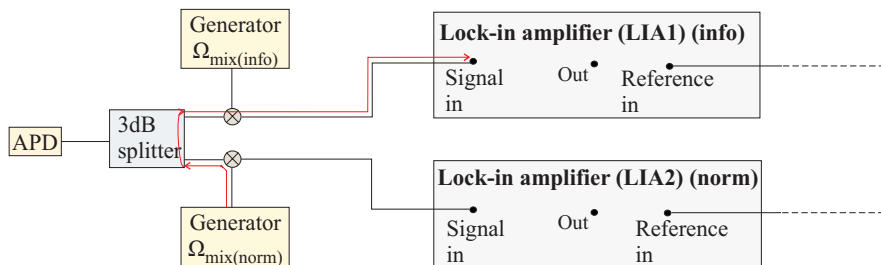

Fig. 16. The detector circuit before modifications.

To block the feedback signal amplifiers were placed in each detector arm as shown in Fig.

Generator
$\Omega_{mix(info)}$

Lock-in amplifier (LIA1) (info)

Signal in   Out   Reference in

APD

3dB splitter

Amplifier

Attenuator

Amplifier

Attenuator

Lock-in amplifier (LIA2) (norm)

Signal in   Out   Reference in
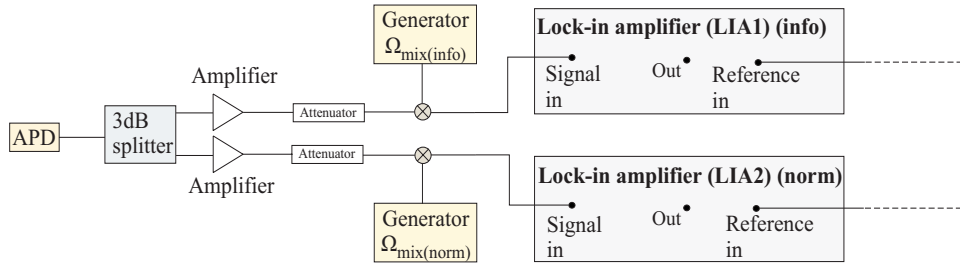
Generator
$\Omega_{mix(norm)}$

Fig. 17. The detector circuit after modifications.

17. Following the amplifiers are attenuators to reduce the signal amplitude to the original level. The feedback signals will now be blocked by the amplifiers and in this way we reduce the noise floor due to interference of the system radically. As mentioned before, feedback into LIA2 is not a problem. We have nevertheless placed amplifiers in both circuit arms to maintain the symmetry.

5.2. The noise floor due to the detector

The detector is a Hamamatsu APD module C5658. The noise level in the dark state is specified to -48dBm at 1GHz detection bandwidth. We assume that the noise has a flat frequency response, i.e. the noise level of the detector is approximately uniform for all frequencies. After being split in half by the power splitter we are left with -51dBm in each detector arm, corresponding to 0.64mV RMS in a 50Ω system. We assume that noise generated from the power splitter can be disregarded. When measuring at 3.3Hz detection bandwidth, which was performed in Fig. 15, this corresponds to a noise level of 6.7nV RMS. This relative amplitude can be recalculated into absolute amplitude, by using Eq. (5): $a = \frac{\lambda}{2\pi} \frac{R_I}{R_N}$. When using the noise level of the detector at 3.3Hz detection bandwidth as R_I, and using the mean value of the R_N measurements obtained in Fig. 15, R_N=0.0447V, the corresponding amplitude is a=0.12pm. The values of R_N are dependent on the reflectivity of the sample. This means that the noise level possible to obtain with our setup is dependent on the reflectivity of the sample. When calculating the noise level of the CMUT membrane we used the mean reflectivity across the sample surface even though there are small variations along the surface.

With our 6pm noise level today we can still reduce the noise level noticeably before reaching the limiting value of the detector.

6. Conclusion

The heterodyne interferometer demonstrated is a flexible setup designed to measure in the entire frequency range 0-1.2GHz with picometer sensitivity. This allows characterization of numerous kinds of devices although we are currently mostly interested in microstructures. The fact that we can retrieve both absolute phase and amplitude, enables the possibility to characterize the total vibration pattern. This will facilitate the understanding of responses of vibrating surfaces including micro- and nanostructures. The lateral resolution is 0.8μm, but can be improved by choosing a lens with higher NA.

The noise floor obtained is $4pm/\sqrt{Hz}$, which satisfies the requirements for the structures we have characterized so far. However, it is desirable to reach even lower amplitudes and we expect to measure in the 10^{-13}m range. This can be done by optimizing both the electrical and optical setup.

Acknowledgments